Arabian Journal for Science and Engineering (2018) 43:6429–6444
https://doi.org/10.1007/s13369-018-3208-0

RESEARCH ARTICLE - PETROLEUM ENGINEERING

Stimulated Reservoir Volume Estimation and Analysis of Hydraulic Fracturing in Shale Gas Reservoir

Lan Ren[1] · Ran Lin[1] · Jinzhou Zhao[1]

Received: 23 February 2017 / Accepted: 20 March 2018 / Published online: 27 March 2018

Abstract

Hydraulic fracturing in horizontal well is the key technology for the commercial exploitation of shale gas reservoir. Stimulated reservoir volume (SRV) is an important indicator to evaluate the fracturing performance. However, estimating the SRV has been a long-standing challenge due to its complex forming mechanism. Most current SRV estimation methods are either expensive or time-consuming. This paper developed a 3D mathematical model to estimate the SRV by simulating the four main processes during shale fracturing—multiple hydraulic fractures propagation, formation stress variation, reservoir pressure lifting and natural fractures failure. In this model, hydraulic fractures propagation is calculated by pseudo-three-dimensional model, coupling with formation stress model; formation stress and reservoir pressure are obtained by displacement discontinuity method and Green's function approach, respectively; natural fracture failure criterion is derived from Warpinski's theory. This model not only considers the stress interference effect of multiple fractures, but also subdivides the SRV into shear-SRV and tensile-SRV according to the failure type of natural fractures network. This model was first implemented to a pilot well in the FL gas field in southwest China to estimate a SRV that matches well with the on-site monitoring microseismic signals. Then, this model was applied to FL gas field on a large scale to evaluate the overall fracturing effects. Finally, a sensitivity study was conducted to analyze the impact of engineering parameters on the SRV. This research explores an efficient method to estimate the SRV without high cost or complicated process and provides the theoretical basis and guidelines for pre-fracturing design and post-fracturing evaluation in shale gas reservoir.

Keywords Shale gas · Hydraulic fracturing · Stimulated reservoir volume · Mathematical modeling · Field application

List of symbols

$(A_{nn})_{ij}$	Plane-strain, elastic-influence coefficient matrix representing the normal stress at element i induced by normal-displacement discontinuity at element j; $i, j \in \{1, 2, \ldots, N\}$
$(A_{nt})_{ij}$	Plane-strain, elastic-influence coefficient matrix representing the normal stress at element i induced by shear-displacement discontinuity at element j; $i, j \in \{1, 2, \ldots, N\}$
$(A_{tn})_{ij}$	Plane-strain, elastic-influence coefficient matrix representing the shear stress at element i induced by normal-displacement discontinuity at element j; $i, j \in \{1, 2, \ldots, N\}$
$(A_{tt})_{ij}$	Plane-strain, elastic-influence coefficient matrix representing the shear stress at element i induced by shear-displacement discontinuity at element j; $i, j \in \{1, 2, \ldots, N\}$
c_L	Filtration coefficient (m/s$^{0.5}$)
E	Young's modulus of formation rock (Pa^{-1})
$\vec{f}$	Force vector imposed on the unit area of fracture surface (Pa)
F_i	Derivatives functions, $i \in \{3, 4, 5, 6\}$,
G	Formation shear modulus (Pa^{-1})
h_f	Fracture height (m)
h_r	Thickness of reservoir (m);
h_{rD}	Dimensionless thickness of reservoir
K_0	Zeroth-order Bessel function
K_f	Friction coefficient of natural fracture

✉ Ran Lin
bob_home@126.com

Lan Ren
renlanswpu@163.com

Jinzhou Zhao
zhaojz@swpu.edu.cn

[1] State Key Laboratory of Oil and Gas Reservoir Geology and Exploitation, Southwest Petroleum University, Chengdu 610500, China

K_{IC}	Fracture toughness (Pa m$^{0.5}$)
k_m	Average permeability of matrix system (D)
k_{mx}	x-Directional permeability of matrix system (D)
L	Arbitrary reference length (m)
L_f	Fracture half-length (m)
M	Number of hydraulic fractures
N	Number of discontinuous fracture elements
n_i	Component of $\vec{n}$, $i \in \{x, y, z\}$
N_{IL}	An even number between 6 and 18
p	Current reservoir pressure (Pa)
p_0	Initial reservoir pressure (Pa)
p_f	Fluid pressure in fracture (Pa)
$p_{f,i}$	Fluid pressure in fracture, $i \in \{1, 2, \ldots M\}$ (m^3/s)
p_{fnet}	Net pressure in fracture (Pa)
p_{nf}	Fluid pressure in natural fracture (reservoir pressure) (Pa)
$\tilde{q}$	Filtration rate per unit area (m/s)
q	Flow rate in fracture (m^3/s)
Q_i	Inlet flow rate of each fracture $i \in \{1, 2, \ldots M\}$ (m^3/s)
Q_{pump}	Pump rate (m^3/s)
s	Laplace transform variable
S_t	Tensile strength of natural fracture (Pa)
t	Time (s)
u	Defined function
$(\hat{u}_n)_i$	Normal strain of element i in local coordinate, $i \in \{1, 2, \ldots N\}$ (m)
$(\hat{u}_t)_i$	Shear strain of element i in local coordinate, $i \in \{1, 2, \ldots N\}$ (m)
W_f	Fracture width (m)
x_D	Dimensionless x value
x_{wD}	Dimensionless x value at perforation point
y_D	Dimensionless y value
y_{wD}	Dimensionless y value at perforation point
z_w	z value at cluster point (m)
α	Integration variable
δ	Kronecker delta
Δp	Pressure increment field in the real domain (Pa)
$\Delta \bar{p}$	Reservoir pressure increment in Laplace domain (Pa)
Δp_i	Pressure increment, induced by fluid leak-off from fracture i, $i \in \{1, 2, \ldots M\}$ (Pa)
$\Delta\sigma_{ij}$	Components of induced stress tensor, $i, j \in \{x, y, z\}$ (Pa);
θ	Approaching angle of natural fracture (°)
φ	Dip angle of natural fracture (°)
μ	Viscosity of fracturing fluid (Pa s)
ν	Poisson ratio
σ_{ij}	Components of current formation stress tensor, $i, j \in \{x, y, z\}$ (Pa)
$\sigma_{ij}^{(0)}$	Components of original formation stress tensor, $i, j \in \{x, y, z\}$ (Pa)
$\vec{\vec{\sigma}}$	Formation stress tensor (Pa)
$(\sigma_n)_i$	Normal stress on element i in local coordinate, $i \in \{1, 2, \ldots N\}$ (Pa)
$(\sigma_t)_i$	Shear stress on element i in local coordinate, $i \in \{1, 2, \ldots N\}$ (Pa)
σ_n	Normal stress imposed on fracture surface (Pa)
σ_τ	Shear stress imposed on natural fracture (Pa)
τ	Start time of filtration in fracture (s)
τ_o	Cohesive strength of natural fracture (Pa)

1 Introduction

In the last decade, as shale gas reservoir has been explored in many countries, global petroleum industry places great importance on this unconventional resource. However, with the ultra-low permeability and low porosity, vertical well drilling followed by conventional hydraulic fracturing is not well performed in the shale gas reservoir [1,2]. Because of the brittleness of shale rock, fortunately, a large number of natural fractures are existing in the reservoir, which can be effectively stimulated by multistage fracturing in horizontal wells [3–5]. This technique can dramatically increase shale gas production and improve the economic efficiency [6,7].

During multistage hydraulic fracturing, the horizontal well is segmented into several stages and pumps a large amount of slick water into reservoir at a high flow rate in each stage. It aims at creating hydraulic fractures and stimulating surrounding natural fractures [8]. Those hydraulic fractures and stimulated natural fractures are interwoven into an activated fractures network, in which the reservoir permeability is substantially increased, and consequently, the gas well production soars [9].

The activated fractures network is often referred to as "stimulated reservoir volume (SRV)" [10]. So far, numerous field data have shown a significant positive correlation between SRV and shale gas production [11,12]; therefore, estimating the SRV is becoming indispensable for pre-fracturing design and post-fracturing evaluation in shale gas reservoir. Currently, there are several ways to estimate SRV, which could be divided into two categories: direct measurement and numerical simulation. Direct measurement methods include microseismic monitoring [13,14] and tiltmeter measurement [15,16]; numerical simulation methods include wire-mesh modeling [17,18] and discrete fracture modeling (DFM) [19–23]. These estimation methods have different advantages and disadvantages: Microseismic monitoring is accurate but costs too much, tiltmeter measurement is cheap but sometimes inaccurate, especially for deep reservoir, wire-mesh modeling is convenient to use but somehow oversimplified, DFM is comprehensive but too complicated, its 3D simulation program usually runs in hours even days.

Thus, a reliable, economical and time-saving SRV estimation method is desiderated for the hydraulic fracturing in horizontal shale gas wells.

This paper established a SRV estimation model by simulating four key processes during shale gas reservoir fracturing: (1) multiple hydraulic fractures propagation; (2) reservoir pressure lifting; (3) formation stress variation; and (4) natural fractures failure. In this model, hydraulic fractures are treated as discrete elements, while natural fractures network is treated as continuous medium, so that the computational burden and computation time can be greatly reduced. This model was applied to the FL shale gas field in southwestern China to validate its feasibility and reliability. Finally, a sensitivity study was conducted to analyze the influence of engineering parameters on the SRV.

2 Mathematical Model

The SRV estimation model comprises three modules and one criterion: hydraulic fracture propagation module, formation stress module, reservoir pressure module and natural fracture failure criterion. The model assumptions include: (1) hydraulic fractures propagate in the vertical plane; (2) fracturing fluid is non-Newtonian fluid; (3) reservoir permeability/porosity is not stress dependent.

2.1 Hydraulic Fracture Propagation

For each fracturing stage in horizontal well, there might be multiple hydraulic fractures initiating from different perforation clusters and propagating simultaneously. Establish a Cartesian coordinate system as Fig. 1 (x-axis: minimum horizontal stress; y-axis: maximum horizontal stress; z-axis: vertical stress).

(1) Fracture flow

Slick water—an incompressible non-Newtonian fluid—is the most common fracturing fluid used in shale gas well fracturing [24]. For the slick water flow in hydraulic fracture, the pressure drop equation along fracture length is simplified from the Navier–Stokes equations [25]:

$$\frac{\mathrm{d}p_{\mathrm{fnet}}(y)}{\mathrm{d}y} = 2^{n'+1}k'\left(\frac{2n'+1}{n'}\right)^{n'} \times \left(\frac{q(y)}{H_{\mathrm{f}}(y)}\right)^{n'} [W_{\mathrm{f}}(y)]^{-(2n'+1)} \tag{1}$$

where k' is the fluid-consistency factor, Pa s; n' is the fluid power-law index, Pa s; $q(y)$ is the flow rate in fracture at y, m^3/s; $W_{\mathrm{f}}(y)$ is the maximum fracture width at y, m; $H_{\mathrm{f}}(y)$ is the fracture height at y, m; $p_{\mathrm{fnet}}(y)$ is the net pressure in fracture at y, Pa; $\sigma_{\mathrm{n}}(y)$ is the normal stress imposed on fracture surface, Pa.

Equation 1 describes the relationship among net pressure drop, flow rate, fluid property and fracture geometry. The fracture net pressure can be obtained by inner pressure minus minimum horizontal stress:

$$p_{\mathrm{fnet}}(y) = p_{\mathrm{f}}(y) - \sigma_{\mathrm{min}} \tag{2}$$

where $p_{\mathrm{f}}(y)$ is the fluid pressure in fracture at y, Pa; σ_{min} is the minimum horizontal stress, Pa.

(2) Fracture geometry

The geometry parameters of hydraulic fracture include its height, width and length. Fracture height can be determined by the fracture toughness and net pressure of fracture [21]:

$$H_{\mathrm{f}}(y) = \frac{2}{\pi}\left(\frac{K_{\mathrm{IC}}}{p_{\mathrm{fnet}}(y)}\right)^2 \tag{3}$$

where K_{IC} is the fracture toughness, $\mathrm{Pa\,m}^{0.5}$.

In the classical elasticity theory, fracture width can be derived by England and Green integral functions [26]:

$$W_{\mathrm{f}}(y) = \frac{2\left(1-\nu^2\right)H_{\mathrm{f}}(y)\,p_{\mathrm{fnet}}}{E} \tag{4}$$

where E is the Young's modulus of formation rock, Pa^{-1}; ν is the Poisson ratio, dimensionless.

However, when multiple fractures propagate simultaneously, they will interfere with each other due to their stress interference effect [27,28], so that the classic equation no longer applies. In this case, multiple fracture widths are obtained by displacement discontinuity boundary method (DDM), see details in Sect. 2.2.

(3) Material balance

The material balance applies to both individual fracture and multiple fractures. For individual fracture, the total flow rate equals to the sum of fluid leak-off volume and fracture volume increment:

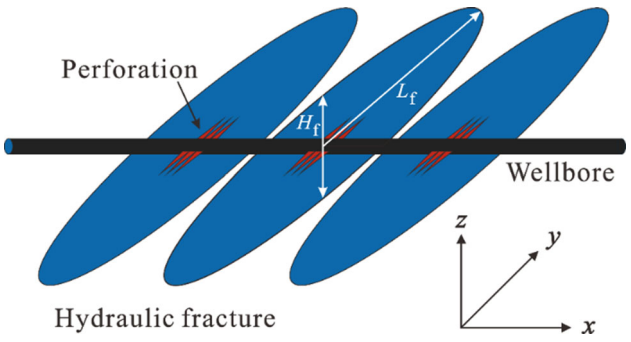

Fig. 1 Single stage of horizontal well fracturing with three clusters

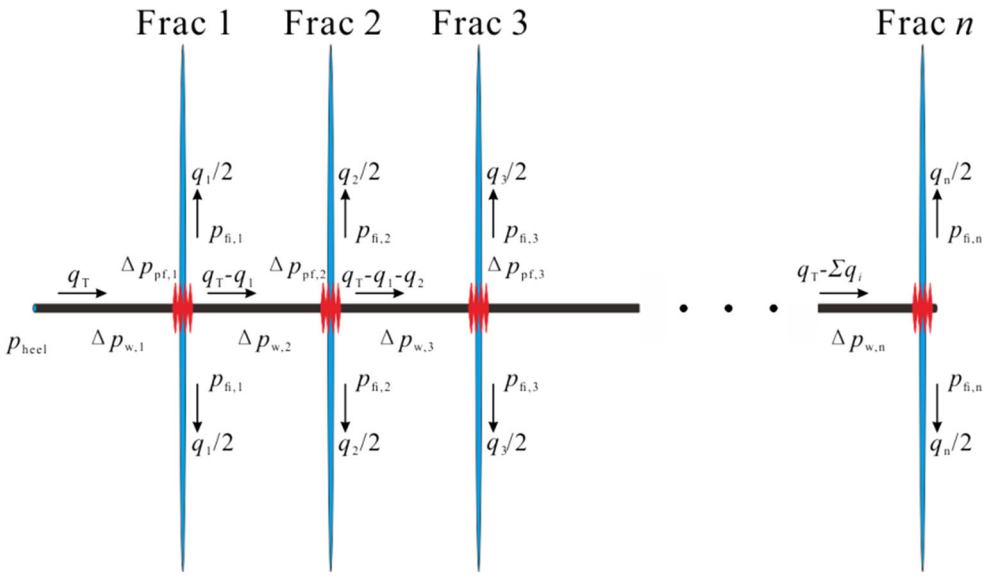

Fig. 2 Flow rate distribution in horizontal wellbore and hydraulic fractures

$$\int_0^t q_f \mathrm{d}t = \int_0^{L_f} \int_0^t \frac{2H_f(y)\, c_L}{\sqrt{t-\tau(y)}} \mathrm{d}t\mathrm{d}y + \int_0^{L_f} H_f W_f \mathrm{d}y \quad (5)$$

where $\tau(y)$ is the start time of leak-off in fracture at y, s; c_L is the filtration coefficient, m/s$^{0.5}$; t is the time, s.

For multiple fractures, the total pumping rate is equal to the sum of inlet flow rate of each fracture:

$$Q_{pump} = \sum_{i=1}^{M} Q_i \quad (6)$$

where Q_{pump} is the pump rate, m^3/s; Q_i is the inlet flow rate of each fracture, m^3/s; M is the number of hydraulic fractures.

(4) Initial and boundary conditions

The initial and boundary conditions of fracture propagation include:

$$\begin{cases} L_f\,|_{t=0} = 0 \\ q_f\,|_{y=0} = Q \end{cases} \quad (7)$$

where Q is the inlet flow rate of fracture, m^3/s; L_f is the fracture half-length, m;

By combining the solution conditions in Eqs. (5)–(8), the geometry of hydraulic fracture can be solved by coupling Eqs. (1)–(3) and (14)–(15) with implicit finite difference method (FDM) [29].

(5) Flow rate distribution

Generally, there are 2–5 perforation clusters for fracture initiation in each fracturing stage, so that multiple hydraulic fractures will propagate simultaneously. Because of the flow friction of fracturing fluid in wellbore and hydraulic fractures (Fig. 2), the inlet flow rate of each hydraulic fracture might be different.

According to Kirchhoff's second law, the pressure at wellbore heel is equal to the sum of wellbore friction pressure drop, perforation friction pressure drop, and the pressure of hydraulic fracture inlet [30]:

$$p_{heel} = p_{fi,i} + \Delta p_{pf,i} + \sum_{j=1}^{i} \Delta p_{w,j} \quad (8)$$

where

$$\Delta p_{pf,i} = 0.135 \frac{q_i^2 \rho}{n_{pf,i}^2 d_{pf,i}^4 \alpha_{pf,i}^2} \quad (9)$$

$$\Delta p_{w,j} = \frac{128\mu}{\pi d_w^4} \sum_{j=1}^{i} L_{w,j} q_{w,j}^{n'} \quad (10)$$

where p_{heel} is the pressure at horizontal wellbore heel, Pa; $\Delta p_{pf,i}$ is perforation friction pressure drop of fracture i, Pa; $\Delta p_{w,j}$ is wellbore friction pressure drop of segment j, Pa; q_{pf} is flow rate at perforation, m^3/s; n_{pf} is perforation number; d_{pf} is perforation diameter, m; α is flow coefficient of perforation, commonly ranged from 0.8 to 0.85, dimensionless; ρ is fracturing fluid density, kg/m^3; μ is fracturing fluid viscosity, mPa·s; $L_{w,j}$ is the length of wellbore segment j, m; d_w is wellbore diameter, m.

The flow rate in each wellbore segment is:

$$q_{w,j} = q_T - \sum_{i=1}^{j-1} q_i \quad (11)$$

where $q_{w,j}$ is the flow rate of wellbore segment j, m^3/s; q_T is total flow rate, m^3/s; q_i is the inlet flow rate of hydraulic fracture i, m^3/s.

According to material balance, one equation can be set up:

$$q_T - \sum_{i=1}^{N} q_i = 0 \tag{12}$$

According to pressure drop formula, N equations can be set up:

$$p_{fi,i} + \Delta p_{pf,i} + \sum_{j=1}^{i} \Delta p_{w,j} - p_{heel} = 0 \quad (i \in 1 \sim N) \tag{13}$$

As above, there are $N+1$ nonlinear equations, and there are $N+1$ unknown parameters (i.e., $q_1, q_2, \ldots, q_N, p_{heel}$). Therefore, the inlet flow rate of each fracture can be solved by building the Jacobian matrix and then applying Newton iteration method.

2.2 Formation Stress

As hydraulic fractures propagate underground, induced stress will be triggered due to the rock deformation, and then, the original formation stress changes accordingly. Based on the elastic mechanics theory, Crouch [31] proposed the displacement discontinuity boundary method (DDM) to describe induced stress variation in infinite elastic materials. This method is especially useful for infinite continuous medium with displacement discontinuity structure such as fracture and cavity [32,33].

Establish the global $x-y$ Cartesian coordinate system as Fig. 3, and discretize all hydraulic fractures into N discontinuous displacement elements. Then establish the local $\xi-\zeta$ coordinate system for each element, and the ξ-axis and ζ-axis are, respectively, parallel and normal to the tangential direction of each discrete element.

According to DDM, the stress equilibrium equations for all discrete fracture elements can be written as:

$$(\sigma_t)_i = \sum_{j=1}^{N} (A_{tt})_{ij} \left(\hat{u}_t\right)_j + \sum_{j=1}^{N} (A_{tn})_{ij} \left(\hat{u}_n\right)_j \tag{14}$$

$$(\sigma_n)_i = \sum_{j=1}^{N} (A_{nt})_{ij} \left(\hat{u}_t\right)_j + \sum_{j=1}^{N} (A_{nn})_{ij} \left(\hat{u}_n\right)_j \tag{15}$$

where $(\sigma_t)_i$ and $(\sigma_n)_i$ are the shear stress and normal stress on element i in local coordinate, Pa; $\left(\hat{u}_t\right)_j$ and $\left(\hat{u}_n\right)_j$ are the shear strain and normal strain on element i in local coordinate, m; $(A_{tt})_{ij}$, $(A_{tn})_{ij}$, $(A_{nt})_{ij}$ and $(A_{nn})_{ij}$ are the plane-strain, elastic-influence coefficient matrix representing the normal/shear stress at element i induced by shear-displacement/normal-displacement discontinuity at element j, respectively; $i, j \in \{1, 2, \ldots, N\}$.

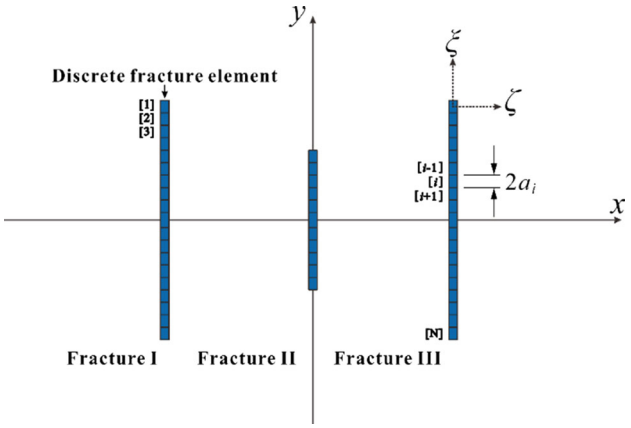

Fig. 3 Multiple hydraulic fractures are discretized into N elements

Hydraulic fractures inner pressure could be obtained from hydraulic fracture propagation module in Sect. 2.1. There should be no shear stress but only normal stress on the fracture surface, so the displacement discontinuity boundary conditions are:

$$(\sigma_t)_i = 0 \tag{16}$$

$$(\sigma_n)_i = -p_{fnet}(y) \tag{17}$$

By combining the boundary conditions, the stress equilibrium Eqs. (14) and (15) can be solved simultaneously to determine the shear and normal strain of each element—$\left(\hat{u}_t\right)_i$, $\left(\hat{u}_n\right)_i$. That $\hat{u}_n$ is equal to the fracture width (W_f), and it can be coupled into hydraulic fracture propagation module (Sect. 2.1) to calculate other geometry parameters.

Then, the induced stress can be calculated by substituting $\left(\hat{u}_t\right)_i$ and $\left(\hat{u}_n\right)_i$ into following formulas:

$$\Delta\sigma_{xx} = \frac{G\hat{u}_n}{2\pi(1-\nu)}\left[2nlF_3 + \left(n^2 - l^2\right)F_4 + \zeta(lF_5 + nF_6)\right] + \frac{G\hat{u}_t}{2\pi(1-\nu)}\left[2n^2F_3 - 2nlF_4 + \zeta(nF_5 - lF_6)\right] \tag{18}$$

$$\Delta\sigma_{yy} = \frac{G\hat{u}_n}{2\pi(1-\nu)}\left[2nlF_3 + \left(n^2 - l^2\right)F_4 - \zeta(lF_5 + nF_6)\right] - \frac{G\hat{u}_t}{2\pi(1-\nu)}\left[2l^2F_3 + 2nlF_4 + \zeta(nF_5 - lF_6)\right] \tag{19}$$

$$\Delta\sigma_{xy} = \frac{G\hat{u}_n}{2\pi(1-\nu)}\zeta(lF_6 - nF_5) + \frac{G\hat{u}_t}{2\pi(1-\nu)}\left[F_4 + \zeta(lF_5 + nF_6)\right] \tag{20}$$

$$\Delta\sigma_{zz} = \nu\left(\Delta\sigma_{xx} + \Delta\sigma_{yy}\right) \tag{21}$$

where $\Delta\sigma_{xx}$, $\Delta\sigma_{yy}$, $\Delta\sigma_{zz}$ and $\Delta\sigma_{xy}$ are the components of induced stress tensor, Pa; G is the formation shear modulus, Pa^{-1}; F_3-F_6 are the derivative functions, dimensionless. The coefficient matrices $(A_{\mathrm{tt}})_{ij}$, etc., derivative functions F_3-F_6 and transformation equation of global–local coordinate are given by Coruch [31].

According to the linear superposition principle of stress tensor, current formation stress can be obtained by superimposing the original formation stress over induced formation stress:

$$\begin{bmatrix} \sigma_{xx} & \sigma_{xy} & \sigma_{xz} \\ \sigma_{yx} & \sigma_{yy} & \sigma_{yz} \\ \sigma_{zx} & \sigma_{zy} & \sigma_{zz} \end{bmatrix} = \begin{bmatrix} \sigma_{xx}^{(0)} + \Delta\sigma_{xx} & \sigma_{xy}^{(0)} & \sigma_{xz}^{(0)} + \Delta\sigma_{xz} \\ \sigma_{yx}^{(0)} & \sigma_{yy}^{(0)} + \Delta\sigma_{yy} & \sigma_{yz}^{(0)} \\ \sigma_{zx}^{(0)} + \Delta\sigma_{xz} & \sigma_{zy}^{(0)} & \sigma_{zz}^{(0)} + \Delta\sigma_{zz} \end{bmatrix} \tag{22}$$

where $\sigma_{ij}^{(0)}$ is the components of original formation stress tensor, Pa; σ_{ij} is the components of current stress tensor, Pa; $i, j \in \{x, y, z\}$.

2.3 Reservoir Pressure

Shale reservoir is often regarded as dual-porosity (matrix + natural fractures) medium with anisotropic characteristics [34,35]. During fracturing, the fracturing fluid constantly infiltrates from hydraulic fractures into surrounding formation and natural fractures, pressurizing the reservoir.

Establish a 3D Cartesian coordinate system as Fig. 4. Assume the hydraulic fracture as a rectangular surface source and then use Green's function approach to derive the analytical equation of reservoir pressure increment in the Laplace domain [36]:

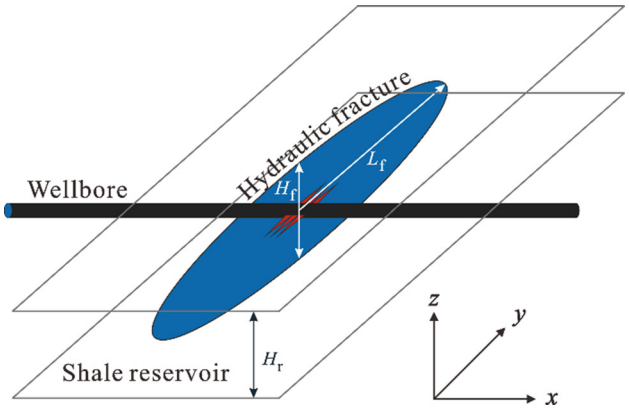

Fig. 4 A hydraulic fracture of horizontal well in the shale gas reservoir

$$\Delta\bar{p}(x, y, z, s) = \frac{2\mu H_{\mathrm{r}}}{\pi k_{\mathrm{m}} h_{\mathrm{rD}} s} \sum_{n=1}^{\infty} \frac{1}{n} \sin n\pi \frac{H_{\mathrm{f}}}{2h_{\mathrm{r}}} \cdot \sin n\pi \frac{z_{\mathrm{w}}}{h_{\mathrm{r}}} \cdot \sin n\pi \frac{z}{h_{\mathrm{r}}} \cdot \int_{-L_{\mathrm{f}}/L}^{+L_{\mathrm{f}}/L} \tilde{q} K_0 \left[\sqrt{u + \frac{n^2\pi^2}{h_{\mathrm{rD}}^2}} \sqrt{\left(x_D - x_{\mathrm{wD}} - \alpha\sqrt{k_{\mathrm{m}}/k_{\mathrm{mx}}}\right)^2 + (y_{\mathrm{D}} - y_{\mathrm{wD}})^2} \right] \mathrm{d}\alpha \tag{23}$$

where $\Delta\bar{p}$ is the reservoir pressure increment in Laplace domain, Pa; L is an arbitrary reference length, m; H_{r} is the thickness of reservoir, m; h_{rD} is the dimensionless thickness of reservoir, dimensionless; k_{mx} is the x-directional permeability of matrix system, D; k_{m} is the average permeability of matrix system, D; $\tilde{q}$ is the filtration rate per unit area, m/s; s is the Laplace transform variable; α is the integration variable, dimensionless; K_0 is the zeroth-order Bessel function; u is a defined function; z_{w} is the z value at cluster point, m; x_{D} is the dimensionless x value, dimensionless; y_{D} is the dimensionless y value, dimensionless; x_{wD} is the dimensionless x value at perforation point, dimensionless; y_{wD} is the dimensionless y value at perforation point, dimensionless. The definitions of function u and dimensionless parameters are given by Ozkan and Raghavan [36].

Through Stehfest [37] numerical inverse approach, the reservoir pressure increment in Laplace domain can be transformed into real domain:

$$\Delta p(x, y, z, t) = \frac{\ln 2}{t} \sum_{i=1}^{N_{\mathrm{IL}}} V_i \Delta\bar{p}\left(x, y, z, \frac{\ln 2}{t} i\right) \tag{24}$$

$$V_i = (-1)^{(N_{\mathrm{IL}}/2+i)} \times \sum_{k=[(i+2)/2]}^{\min(i, N_{\mathrm{IL}}/2)} \frac{k^{N_{\mathrm{IL}}/2+1}(2k)!}{(N_{\mathrm{IL}}/2-k)!k!(k-1)!(i-k)!(2k-i)!} \tag{25}$$

where $\Delta p(x, y, z, t)$ is the pressure increment field in the real domain, Pa; N_{IL} is an even number between 6 and 18.

According to the linear superposition principle of pressure, when multiple hydraulic fractures coexist in the reservoir, current reservoir pressure field can be obtained by superimposing the initial reservoir pressure field over pressure increment field:

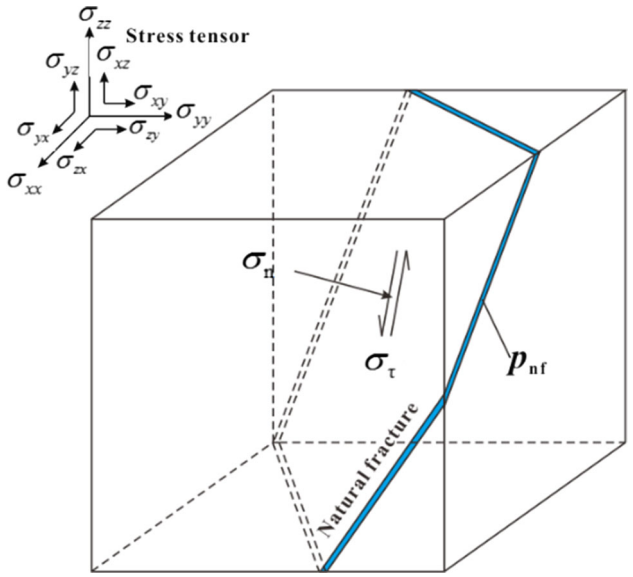

Fig. 5 Stress analysis on natural fracture surface

$$p\,(x, y, z, t) = p_0\,(x, y, z, t_0) + \sum_{i=1}^{M} \Delta p_i\,(x, y, z, t) \tag{26}$$

where p is the current reservoir pressure field, Pa; p_0 is the initial reservoir pressure field, Pa; Δp_i is the pressure increment field, induced by fluid leak-off from fracture i, Pa.

2.4 Natural Fracture Failure Criterion

Because of the brittleness of shale formation, there are often lots of natural fractures developed in shale gas reservoir, and most natural fractures tend to align along a single axis [25,38]. As reservoir pressure and formation stress change during hydraulic fracturing, some natural fractures might occur shear failure (slipping) or tensile failure (opening). These shear-failure and tensile-failure fractures would interweave into activated fractures network, forming the shear-SRV and tensile-SRV, respectively.

Previous natural fracture failure criterion only applies to vertical fracture without considering its dip angle [39]. Based on Warpinski's [40] theory, we derived a more general failure criterion for inclined natural fracture (Fig. 5).

Suppose the unit normal vector of the natural fracture plane is:

$$\vec{\boldsymbol{n}} = n_i e_i = \lfloor n_x\ n_y\ n_z \rfloor \tag{27}$$

$$n_x = \sin(\varphi) \cdot \cos(\theta), n_y = \sin(\varphi) \cdot \sin(\theta), n_x = \cos(\varphi) \tag{28}$$

where n_i is the component of unit normal vector $\vec{\boldsymbol{n}}$, dimensionless, $i \in \{x, y, z\}$; θ is the approaching angle of natural fracture, °; φ is the dip angle of natural fracture, °; $i \in \{x, y, z\}$.

The force imposed on the unit area of fracture surface is:

$$\vec{\boldsymbol{f}} = \vec{\boldsymbol{\sigma}} \cdot \vec{\boldsymbol{n}} = \sigma_{ij} e_i e_j \cdot n_k e_k = \sigma_{ij} n_k e_i \delta_j^k = \sigma_{ij} n_j e_i \tag{29}$$

where $\vec{\boldsymbol{f}}$ is the force vector imposed on the unit area of fracture surface (Pa); $\vec{\boldsymbol{\sigma}}$ is the formation stress tensor, Pa; δ is the Kronecker delta; $i, j, k \in \{x, y, z\}$.

Then, decompose the force along the normal and shear direction of natural fracture plane to obtain its normal and shear stress value, respectively:

$$\sigma_n = \vec{\boldsymbol{f}} \cdot \vec{\boldsymbol{n}} = n_k e_k \cdot \sigma_{ij} n_j e_i = n_k \sigma_{ij} n_j \delta_i^k = n_i \sigma_{ij} n_j \tag{30}$$

$$\sigma_\tau = \sqrt{\vec{\boldsymbol{f}} \cdot \vec{\boldsymbol{f}} - \sigma_n^2} = \sqrt{\sigma_{ij} n_j e_i \cdot \sigma_{ij} n_j e_i - \sigma_n^2} = \sqrt{\sigma_{ij} n_j \sigma_{ij} n_j - \sigma_n^2} \tag{31}$$

where σ_n is the normal stress value imposed on natural fracture, Pa; σ_τ is the shear stress value imposed on natural fracture, Pa.

Based on Warpinski's theory, the tensile failure criterion for fracture is:

$$p_{nf} > \sigma_n + S_t \tag{32}$$

And the shear failure criterion for fracture is:

$$\sigma_\tau > \tau_o + K_f \cdot (\sigma_n - p_{nf}) \tag{33}$$

where K_f is the friction coefficient of natural fracture, dimensionless; p_{nf} is the fluid pressure in natural fracture, equaling to the current reservoir fluid pressure (p), Pa; S_t is the tensile strength of natural fracture, Pa; τ_o is the cohesive strength of natural fracture, Pa.

Given the reservoir pressure, formation stress and natural fractures orientation, the failure state of natural fractures can be predicted by Eqs. (32) and (33).

2.5 Calculation Workflow

The SRV estimation model is established by integrating those three modules (Sects. 2.1–2.3) and one criterion (Sect. 2.4). The flowchart in Fig. 6 illustrates the calculation steps of this model.

1. Input relevant data (e.g., reservoir parameters, geological parameters, fracturing parameters, etc.) and establish a 3D Cartesian coordinate system;
2. Couple the HF propagation module and stress module (coupling parameter: p_f and W_f) to determine the HF geometry parameters (W_f, h_f, L_f) and formation stress distribution (σ_{ij});

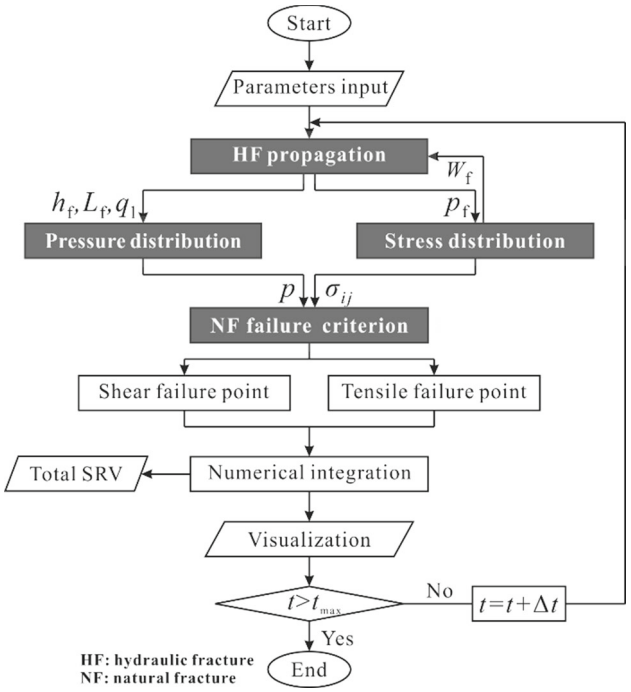

Fig. 6 Workflow of numerical calculation

3. According to HF geometry and fluid filtration volume during fracturing, calculate the reservoir pressure distribution (p) through pressure module;
4. Substitute the formation stress (σ_{ij}) and reservoir pressure (p) into NF failure criterion to predict the NF failure state and failure type (shear failure or tensile failure) at any point of the reservoir and then save their coordinates data;
5. Based on the coordinates data of all failure points, calculate the shear failure volume (shear-SRV) and tensile failure volume (tensile-SRV) by numerical volume integration, then regard the combination of shear-SRV and tensile-SRV as the total-SRV;
6. Visualize the 3D SRV and determine whether current time exceeds the fracturing operation time (t_{max}), if no, move on to the next time step; if yes, end the calculation.

3 Field Application

In order to validate the feasibility and reliability of the SRV estimation model, it has been applied to Fuling (FL) shale gas field.

FL shale gas field is the first major commercial shale gas reservoir outside of North America. It is located in Sichuan Basin, southwest China, with proven gas reserves of more than 99×10^9 m^3 lying in lower Paleozoic Wufeng and Longmaxi marine shale layers [41]. Similar to those successful shale gas fields in North America (e.g., Barnet Shale, Eagle Ford Shale), horizontal well drilling followed by multistage multi-cluster fracturing is the main development method to increase gas production in this field.

Table 1 Geological and fracturing parameters of J–X well

Parameter	Value(s)	Unit
TOC	3.55%	–
Brittle index	67.30%	–
Thermal maturity	2.58%	–
Thickness	38	m
Depth	2538–2576	m
Initial reservoir pressure	38	MPa
Porosity	0.051	–
Permeability of matrix system	0.05	mD
Permeability of NF system	25	mD
Maximum horizontal stress	61.5	MPa
Minimum horizontal stress	52.4	MPa
Vertical stress	58.5	MPa
Cohesive strength of NF	1	MPa
Tensile strength of NF	0.5	MPa
Friction coefficient of NF	0.4	–
Approaching angle of NF	37	°
Dip angle of NF	62	°
Young's modulus	32	GPa
Poisson ratio	0.26	–
Viscosity of fracturing fluid	9	mPa · s
Pump rate	13	m^3/min
Pump duration	123	min
Cluster spacing	30	m
Number of cluster	3	Number

NF natural fracture

3.1 SRV Analysis of Single Fracturing Stage

The SRV estimation model was first applied to the first fracturing stage of a pilot horizontal well (J–X) in FL shale gas field; the geological and fracturing parameters that obtained from field test and laboratory measurement are listed in Table 1.

The hydraulic fractures geometry, reservoir pressure, formation stress and SRV were obtained by program computation, with a running time of 587.62 s.

During fracturing treatment, three hydraulic fractures are propagated in the formation simultaneously. However, because of the stress interference among hydraulic fractures, interior fracture (fracture 2) width was suppressed, increasing its inner pressure gradient as well as inlet pressure. According to the flow rate distribution equation (Eq. 8), the inlet flow rate of interior fracture should be lower than exterior fractures

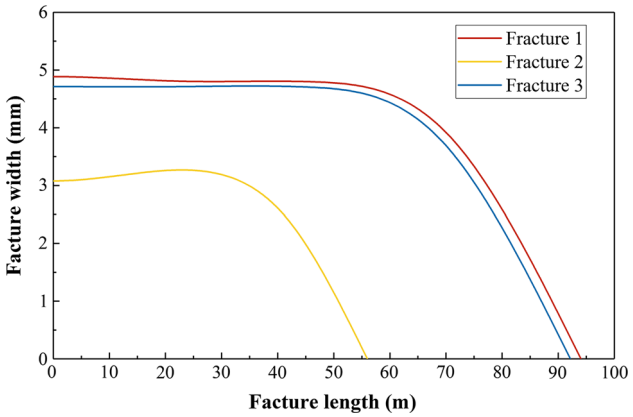

Fig. 7 Fracture width versus fracture length (fractures 1–3: hydraulic fractures from upstream to downstream)

(fractures 1 and 3). Consequently, the interior fracture propagation was constrained. In this case, each hydraulic fracture width is shown in Fig. 7. It shows that interior fracture width ($\sim$ 3.0 mm) is obviously less than exterior fracture width ($\sim$ 4.7 mm), and the exterior fracture half-length is $\sim$ 93 m, while the interior fracture length is restricted to 56 m. Furthermore, because of the flow friction of fracturing fluid in wellbore, the inlet flow rate of upstream fracture (fracture 1) is slightly higher than the downstream fracture (fracture 3), making it slightly longer and wider.

Figure 8 shows the reservoir pressure and formation stress distribution. Original formation stress, including normal stress (σ_x, σ_y) and shear stress (σ_{xz}), was dramatically perturbed by hydraulic fractures, whose induced stress can make natural fractures slip, triggering shear failure. Meanwhile, due to the fracturing fluid filtration, the pressure of surrounding reservoir was elevated. High reservoir pressure can counteract the normal stress on natural fractures surface, triggering tensile failure.

According to calculation results, the shear-SRV and tensile-SRV are 2.44×10^6 and 1.98×10^6 m^3, respectively, and their combination—total-SRV—is 2.92×10^6 m^3 (see in Fig. 9). In most cases, natural fractures need higher net pressure to occur tensile failure than shear failure, so the shear-SRV is usually larger than tensile-SRV. Furthermore, because the natural fractures in this reservoir are not strictly vertical (dip angle $= 62°$), the shape of SRV is slightly tilted.

Microseismic monitoring has been applied in J–X well to estimate the activated fractures network during hydraulic fracturing. When natural fractures such as shear failure occur, a series of micro-earthquake will be triggered and their seismic waves will spread out underground. As these microseismic signals are recorded by adjacent seismometers, the shear failure locations can be pinpointed by seismic inversion method. Therefore, we compared the calculated shear-SRV contour with on-site monitoring microseismic signals, which are shown in Fig. 10 from different perspectives, respectively.

Based on statistical analysis, 85.3% of microseismic signals reside within the contour of calculated shear-SRV. Furthermore, the tilted state of SRV is consistent with the non-axisymmetric distribution of microseismic signals as in Fig. 8c. In summary, the calculated shear-SRV matches well with monitoring microseismic signals.

3.2 SRV Estimation for Single Well

Then, take the X2-HF well for an example to illustrate the SRV estimation of a single well. X2-HF well is located in the northeast of FL gas field, targeting in Wufeng formation and Longmaxi formation with 1447 m horizontal interval. The average depth of its fractured interval is 2561 m, maximum horizontal stress is 58−59 MPa, minimum horizontal stress is 52−53 MPa, vertical stress is 63−64 MPa, Young's modules is 32−37 GPa, Poisson's ratio is 0.22−0.25, many vertical natural fractures are found in cores. In September 2013, this well was fractured in 15 separate stages (3 clusters within each stage), it pumped 28, 650 m^3 slick water and 773.4 m^3 proppants, including 100-mesh ceramic proppant, 40/70-mesh and 30/50-mesh coated sand, into the formation. The specific fracturing parameters of each stage are listed in Table 2.

Based on these fracturing data and SRV estimation model, the SRV of X2-HF well was calculated. The SRV geometry of each fracturing stage is listed in Table 3. For single fracturing stage, the average length, width, height and volume of SRV are 334, 101, 75 m and 1.52×10^6m^3, respectively.

Then, the SRV can be visualized in three dimension by embedding its coordinates data into the geologic model of FL shale gas field. According to the 3D SRV scatter diagram in Fig. 11, the surrounding reservoir of X2-HF well has been fully stimulated by multistage fracturing, with a total-SRV volume of 19.5×10^6m^3.

After the fracturing of X2-HF well, the productivity test showed that its open-flow potential reached to 81.9×10^4 m^3/d, confirmed the effectiveness and efficiency of hydraulic fracturing. The calculated SRV was embedded into a shale gas well production simulation model, which is developed by [42], to predicate the gas production of fractured X2-HF well. The simulation result accords with the field production data (Fig. 12).

3.3 SRV Distribution in FL Shale Gas Field

So far, the SRV estimation model has been applied to 93 wells in FL shale gas field. According to the calculation results, the SRV statistical histogram and distribution map of 93 fractured horizontal wells are illustrated in Figs. 13 and 14, respectively.

Figure 13 indicates that the most wells' SRV range from $(20-40) \times 10^6$m^3, guaranteed the commercial production of

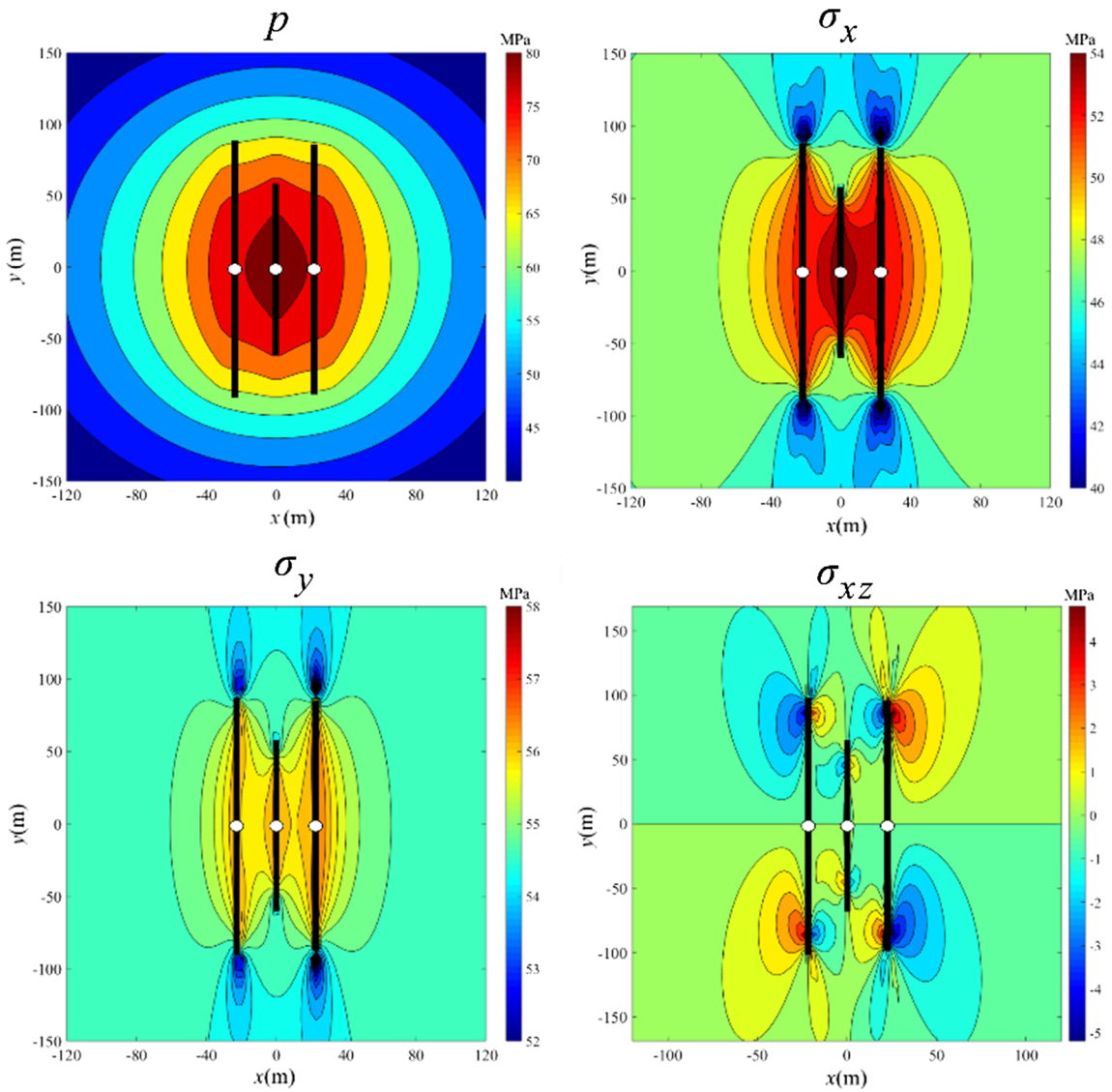

Fig. 8 Reservoir pressure and formation stress distribution

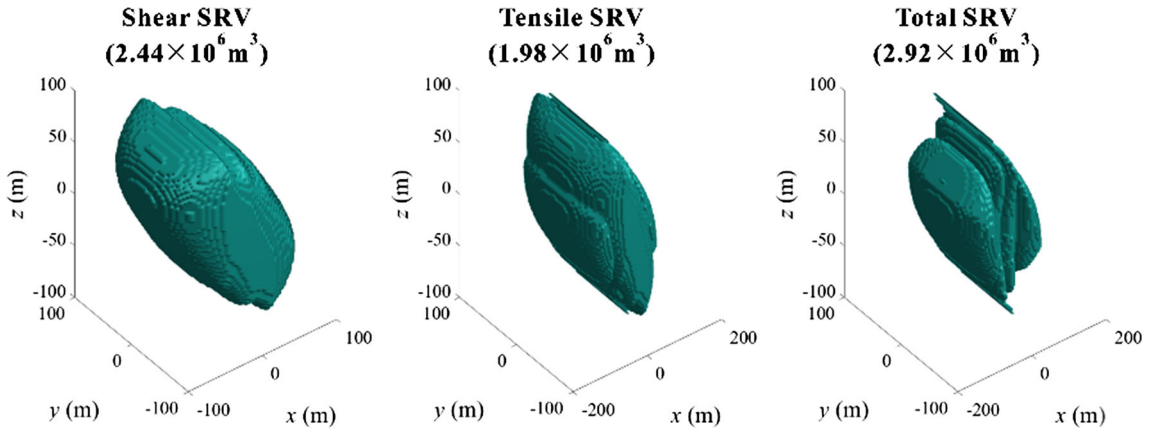

Fig. 9 3D diagram of stimulated reservoir volume (SRV)

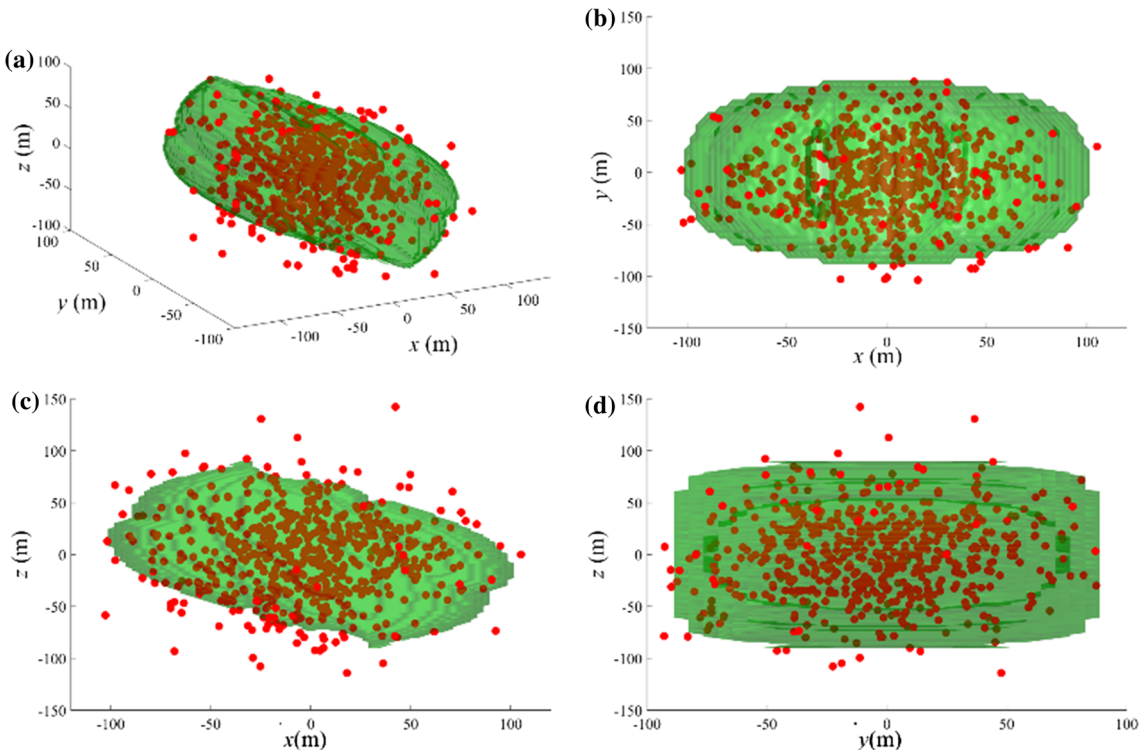

Fig. 10 Comparison of calculated shear-SRV (black line) and microseismic signal (red dots) **a** 3D, **b** x–y plane, **c** x–z plane, **d** y–z plane

Table 2 Fracturing parameters of X2-HF well in FL shale gas field

Stage	Pump rate (m^3/min)	Fluid volume (m^3)	Proppant volume (m^3)	Fluid viscosity (mPa · s)	Cluster spacing (m)
1	14.00	1633.83	60.23	6.50	34, 29
2	14.00	1716.06	58.52	6.50	30, 30
3	14.00	1362.90	23.85	6.50	31, 32
4	12.10	2302.24	30.00	6.50	32, 33
5	12.30	1708.33	61.99	6.50	32, 31
6	13.00	1735.82	75.29	6.50	29, 31
7	12.30	1913.60	81.80	6.50	32, 32
8	12.10	1399.76	52.51	6.50	30, 50
9	12.10	1800.99	44.05	6.50	30, 30
10	13.40	2240.93	36.57	6.50	31, 30
11	12.10	2049.87	50.84	6.50	31, 29
12	12.10	1930.42	49.86	6.50	32, 33
13	12.20	1902.11	46.67	6.50	40, 31
14	12.10	1790.31	50.40	6.50	32, 30
15	12.40	1853.02	50.79	6.50	29, 30

shale gas. However, Fig. 14 shows that there are still unstimulated regions left between adjacent wells, so it could drill infill wells in these blank regions and reduce the well spacing from 600 m now to $\sim$ 450 m to enhance the reservoir recovery and improve the economic efficiency of FL shale gas field.

4 Sensitivity Analysis

In order to optimize the future fracturing design in FL shale gas field, a sensitivity study was conducted to analyze the impact of several engineering parameters on the SRV, including fracturing fluid volume, pump rate, hydraulic fractures number, and perforation cluster spacing.

Table 3 SRV geometry of each fracturing stage in X2-HF well

Stage	SRV length (m)	SRV width (m)	SRV height (m)	SRV volume (10^6 m^3)
1	338.97	97.46	76.86	1.36
2	356.94	104.74	76.17	1.44
3	315.09	72.31	76.21	0.99
4	344.56	100.29	73.53	1.94
5	323.36	100.26	73.32	1.43
6	329.03	98.31	74.60	1.47
7	379.83	113.11	76.55	1.68
8	333.74	55.61	75.67	0.86
9	332.31	111.34	75.35	1.59
10	360.57	109.33	76.95	1.91
11	339.37	113.70	76.95	1.71
12	328.83	110.17	74.56	1.72
13	325.17	108.94	73.73	1.69
14	294.38	112.72	76.29	1.53
15	315.86	112.88	76.40	1.60

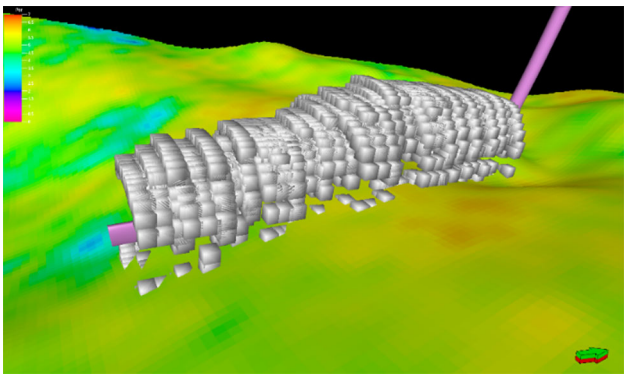

Fig. 11 SRV coordinates data (white dots) of X2-HF well embedded into geologic (porosity) model

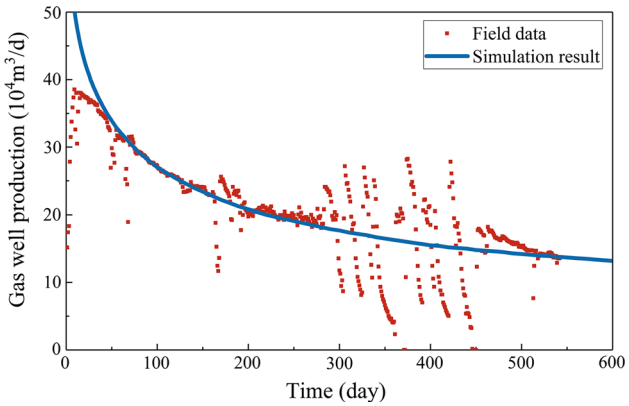

Fig. 12 The production simulation result and field production data of X2-HF well

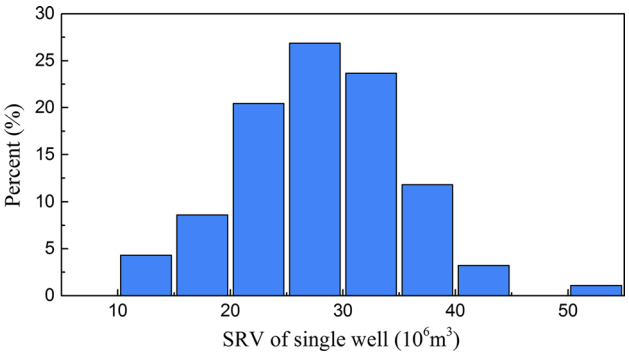

Fig. 13 SRV statistical histogram for each well in FL shale gas field

The SRV with varying fracturing fluid volumes is plotted in Fig. 15. It shows that the SRV increases with fracturing fluid volume. The reason is that more fracturing fluid will create longer hydraulic fractures, resulting in more fluid leak-off to pressurize nearby reservoir. Consequently, more evident pressure lifting makes the reservoir more vulnerable to be stimulated with tensile failure. Therefore, larger fracturing fluid volume is beneficial to enlarge the SRV.

The SRV with varying pump rates is plotted in Fig. 16. It shows that the SRV increases with pump rate. The reason is that the higher pump rate leads to higher net pressure in hydraulic fractures, facilitating the formation stress disturbance. Consequently, more drastic stress changing makes the reservoir more vulnerable to be stimulated with shear failure. Therefore, higher pump rate is preferred to enlarge the SRV.

The SRV with different hydraulic fractures number is plotted in Fig. 17. It shows that there could be an optimal fractures number to maximize the SRV. The reason is that too few hydraulic fractures cannot trigger sufficient stress interference effect to generate large stress disturbance zone, resulting in an undersized SRV. On the other hand, too many fractures will reduce the flow rate as well as net pressure in each fracture; it also impedes the SRV expansion. In this case, three hydraulic fractures can not only induce evident stress interference but also generate adequate net pressure in each fracture, leading to a maximum SRV.

The SRV with varying perforation cluster spacings is calculated and plotted in Fig. 18. It shows that with the increase in cluster spacing, the SRV increases first and then decreases. When cluster spacing is too small, the SRV of each hydraulic fracture will excessively overlap with each other. Conversely, when cluster spacing is too large, the SRV of each hydraulic fracture will completely separate with each other, leaving unstimulated regions. Therefore, there should be an optimal cluster spacing, which makes the SRV of each hydraulic fracture is in a transition stage between excessively overlap and completely separate, to maximize the SRV. In this case, the optimal cluster spacing is 30 m.

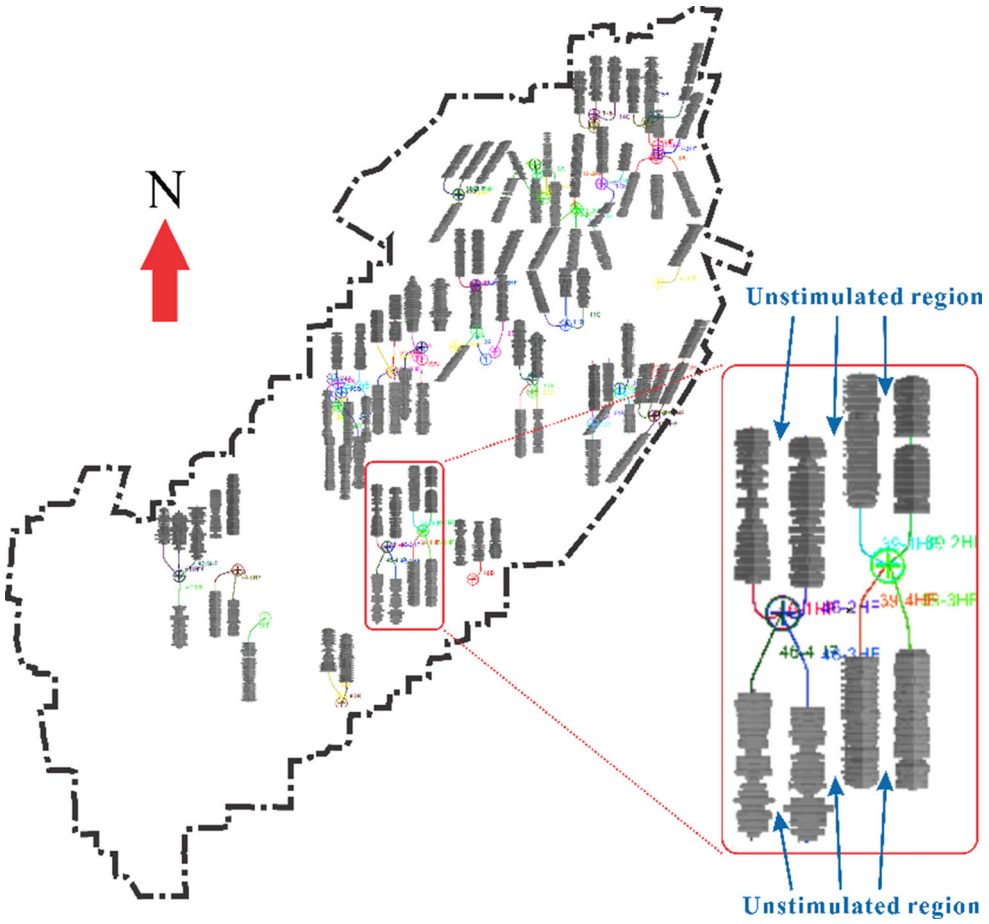

Fig. 14 SRV distribution in FL shale gas field

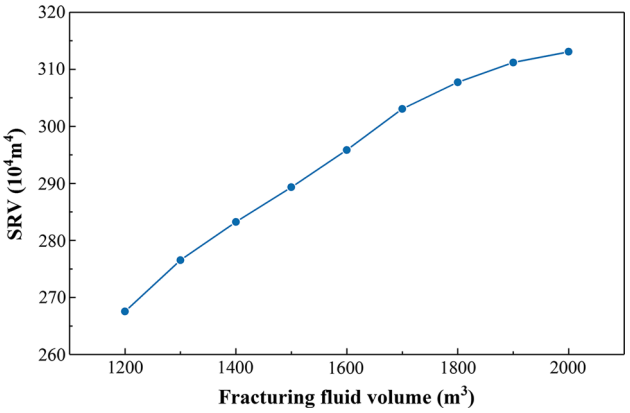

Fig. 15 Impact of fracturing fluid on the SRV

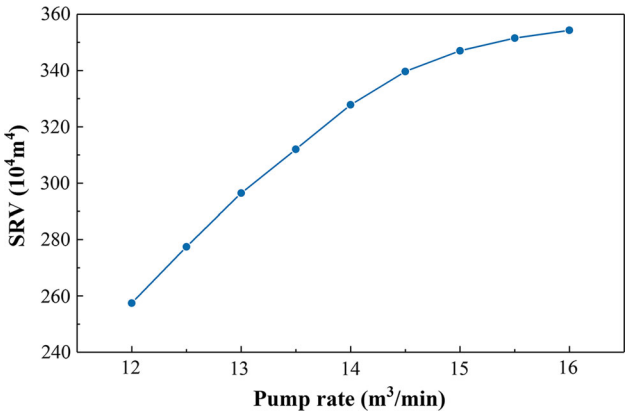

Fig. 16 Impact of pump rate on the SRV

5 Discussion

The SRV estimation model was established by simulating multiple fractures propagation and predicting the natural fractures failure based on geo-stress and reservoir pressure change during hydraulic fracturing in shale gas reservoir. This model has considered some unique physical mechanisms that involved in the shale fracturing, including multiple fractures propagation under stress interference, unequal flow rate distribution among each hydraulic fracture, different failure types of natural fractures, etc. However, the model is somewhat simplified in order to speed up its calculation program, so some factors have not been considered in this paper yet.

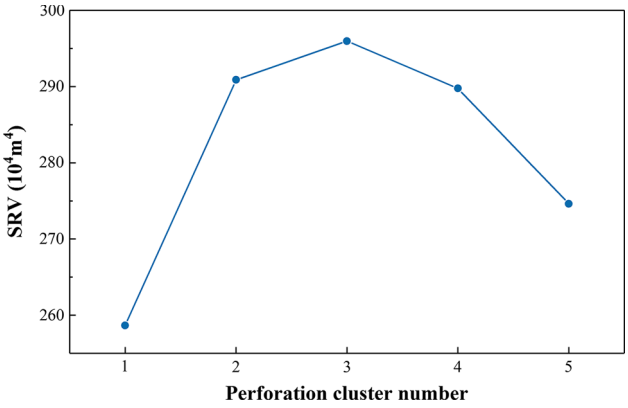

Fig. 17 Impact of hydraulic fracture number on the SRV

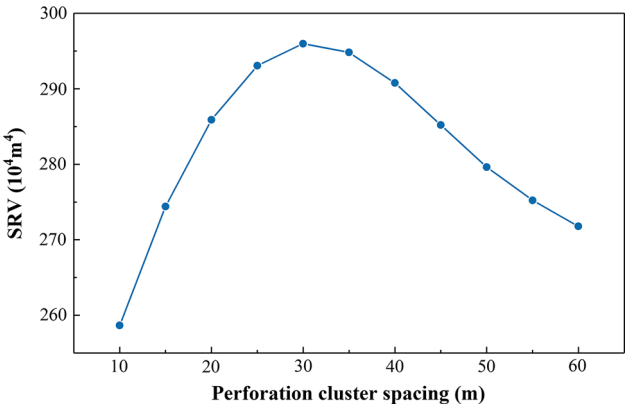

Fig. 18 Impact of perforation cluster spacing on the SRV

For instance, multiple hydraulic fractures might not always propagate in an ideal plane; because of the stress interference effect, fractures might propagate away with each other, resulting in non-planar propagation behavior. Consequently, the SRV might slightly extend its width (the direction along wellbore) while shrink its length (the direction vertical to wellbore). For such case, the cluster spacing between neighboring fracturing stages should be enlarged accordingly. Besides, according to some laboratory tests on core permeability, the pore-pressure and geo-stress might affect the matrix permeability of shale rock, and it could alter the pressure transmission in reservoir, so the SRV would be slightly different from our prediction. In addition, the hydraulic fracture propagation module and formation stress module are both based on linear elastics model, but the mechanical characteristics of actual rock are not always conformed to linear elastics behavior; especially in deep reservoir, both pressure and temperature are high, so the plastic characteristic of shale rock become more obvious, which might impede the hydraulic fractures propagation as well as the SRV expansion. Hence, the elastic–plastic model should be employed to estimate the SRV in high-pressure and/or high-temperature shale reservoir.

As above, all those factors might affect the fracture propagation, formation stress, and reservoir pressure and then eventually change the SRV. In our future research, we will focus those factors, embed them into SRV estimation model, and investigate their influence on SRV, thoroughly.

6 Conclusions

(1) For the hydraulic fracturing in horizontal shale gas well, this paper establishes a 3D mathematical model for SRV estimation by simulating the four key processes: multiple hydraulic fractures propagation, reservoir pressure lifting, formation stress variation, and natural fractures failure.

(2) For each fracturing stage with multiple perforation clusters, several hydraulic fractures will propagate simultaneously, and the interior hydraulic fracture will be restrained by stress interference from exterior fractures. Meanwhile, as reservoir pressure and formation stress change during hydraulic fracturing, some natural fractures might occur shear or tensile failure. These shear-failure and tensile-failure fractures would interweave into activated fractures network, forming the shear-SRV and tensile-SRV, respectively.

(3) This model was first implemented to a pilot well in the FL gas field in southwest China to estimate a SRV that matches well with the on-site monitoring microseismic signals. Then, this model was applied to FL gas field on a large scale; the application results show that although most horizontal wells have been effectively fractured with desired SRV, there are still unstimulated regions left between neighboring wells, so it could drill infill wells in current well pattern and reduce the well spacing in the future.

(4) Sensitivity analysis indicates that engineering parameters, including fracturing fluid volume, pump rate, hydraulic fractures number, and perforation cluster spacing, all have evident influence on the SRV. Hence, those parameters should be carefully designed to maximize the SRV and improve the fracturing performance.

(5) This research explores a convenient method to estimate the SRV without high economical and computational cost. Admittedly, some factors that might also affect the SRV have not been considered in this paper and required further research. Our future study will focus on the non-planar fracture propagation, dependent permeability, elastic–plastic characteristics of shale rock to further improve this SRV estimation model.

Acknowledgements The authors would like to acknowledge the financial support of the Major Program of the National Natural Science Foundation of China (51490653), National Natural Science Founda-

tion of China (51404204), and the National Science and Technology Major Project of the Ministry of Science and Technology of China (2016ZX05023005-001-002).

References

1. Luffel, D.L.; Hopkins, C.W.; Schettler, P.D., Jr.: Matrix permeability measurement of gas productive shales. In: Paper SPE 26633 Presented at the SPE Annual Technical Conference and Exhibition, Houston, Texas (1993). https://doi.org/10.2118/26633-MS
2. Sakhaee-Pour, A.; Bryant, S.: Gas permeability of shale. SPE Reserv. Eval. Eng. **15**(04), 401–409 (2012). https://doi.org/10.2118/146944-pa
3. Ben, Y.; Miao, Q.; Wang, Y.; Shi, G.-h.: Effect of Natural Fractures on Hydraulic Fracturing. In: Paper ISRM-ARMS7-2012-087 Presented at the ISRM Regional Symposium—7th Asian Rock Mechanics Symposium, Seoul, Korea (2012)
4. Cho, Y.; Ozkan, E.; Apaydin, O.G.: Pressure-dependent natural-fracture permeability in shale and its effect on shale-gas well production. SPE Reserv. Eval. Eng. **16**(02), 216–228 (2013). https://doi.org/10.2118/159801-PA
5. Hu, D.; Matzar, L.; Martysevich, V.N.: Effect of natural fractures on eagle ford shale mechanical properties. In: Paper SPE 170651 Presented at the SPE Annual Technical Conference and Exhibition, Amsterdam, The Netherlands (2014). https://doi.org/10.2118/170651-MS
6. King, G.E.: Thirty years of gas shale fracturing: what have we learned? In: Paper SPE 133456 Presented at the SPE Annual Technical Conference and Exhibition, Florence, Italy (2010). https://doi.org/10.2118/133456-MS
7. Wu, Q.; Xu, Y.; Wang, X.; Wang, T.; Zhang, S.: Volume fracturing technology of unconventional reservoirs: connotation, design optimization and implementation. Pet. Explor. Dev. **39**(3), 377–384 (2012). https://doi.org/10.1016/S1876-3804(12)60054-8
8. Zhao, Y.L.; Zhang, L.H.; Luo, J.X.; Zhang, B.N.: Performance of fractured horizontal well with stimulated reservoir volume in unconventional gas reservoir. J. Hydrol. **512**, 447–456 (2014). https://doi.org/10.1016/j.jhydrol.2014.03.026
9. Ge, J.; Ghassemi, A.: Stimulated reservoir volume by hydraulic fracturing in naturally fractured shale gas reservoirs. In: Paper ARMA-2012-468 Presented at the 46th U.S. Rock Mechanics/Geomechanics Symposium, Chicago, Illinois (2012)
10. Fisher, M.K.; Wright, C.A.; Davidson, B.M.; Goodwin, A.K.; Fielder, E.O.; Buckler, W.S.; Steinsberger, N.P.: Integrating fracture mapping technologies to optimize stimulations in the Barnett shale. In: Paper SPE 77441 Presented at the SPE Annual Technical Conference and Exhibition, San Antonio, Texas (2002). https://doi.org/10.2118/77441-MS
11. Mayerhofer, M.J.; Lolon, E.P.; Youngblood, J.E.; Heinze, J.R.: Integration of microseismic-fracture-mapping results with numerical fracture network production modeling in the Barnett Shale. In: Paper SPE 102103 Presented at the SPE Annual Technical Conference and Exhibition, San Antonio, Texas, USA (2006). https://doi.org/10.2118/102103-MS
12. Mayerhofer, M.J.; Lolon, E.; Warpinski, N.R.; Cipolla, C.L.; Walser, D.W.; Rightmire, C.M.: What is stimulated reservoir volume? SPE Prod. Oper. **25**(01), 89–98 (2010). https://doi.org/10.2118/119890-PA
13. Maxwell, S.C.; Urbancic, T.I.; Steinsberger, N.; Zinno, R.: Microseismic imaging of hydraulic fracture complexity in the Barnett Shale. In: Paper SPE 77440 Presented at the SPE Annual Technical Conference and Exhibition, San Antonio, Texas (2002). https://doi.org/10.2118/77440-MS
14. Fisher, M.K.; Wright, C.A.; Davidson, B.M.; Steinsberger, N.P.; Buckler, W.S.; Goodwin, A.; Fielder, E.O.: Integrating fracture mapping technologies to improve stimulations in the Barnett shale. SPE Prod. Facil. **20**(02), 85–93 (2005). https://doi.org/10.2118/77441-pa
15. Griffin, L.G.; Wright, C.A.; Demetrius, S.L.; Blackburn, B.D.; Price, D.G.: Identification and implications of induced hydraulic fractures in waterfloods: case history HGEU. In: Paper SPE 59525 Presented at the SPE Permian Basin Oil and Gas Recovery Conference, Midland, Texas (2000). https://doi.org/10.2118/59525-MS
16. Astakhov, D.; Roadarmel, W.; Nanayakkara, A.: A new method of characterizing the stimulated reservoir volume using tiltmeter-based surface microdeformation measurements. In: Paper SPE 151017 Presented at the SPE Hydraulic Fracturing Technology Conference, The Woodlands, Texas, USA (2012). https://doi.org/10.2118/151017-MS
17. Yu, G.; Aguilera, R.: 3D analytical modeling of hydraulic fracturing stimulated reservoir volume. In: Paper SPE 153486 Presented at the SPE Latin America and Caribbean Petroleum Engineering Conference, Mexico City, Mexico (2012). https://doi.org/10.2118/153486-MS
18. Maulianda, B.T.; Hareland, G.; Chen, S.: Geomechanical consideration in stimulated reservoir volume dimension models prediction during multi-stage hydraulic fractures in horizontal wells—Glauconite tight formation in Hoadley field. In: Paper ARMA 2014-7449 Presented at the 48th U.S. Rock Mechanics/Geomechanics Symposium, Minneapolis, Minnesota (2014)
19. Rogers, S.; Elmo, D.; Dunphy, R.; Bearinger, D.: Understanding hydraulic fracture geometry and interactions in the Horn River Basin through DFN and numerical modeling. In: Paper SPE 137488 Presented at the Canadian Unconventional Resources and International Petroleum Conference, Calgary, Alberta, Canada (2010). https://doi.org/10.2118/137488-MS
20. Meyer, B.R.; Bazan, L.W.: A discrete fracture network model for hydraulically induced fractures—theory, parametric and case studies. In: Paper SPE 140514 Presented at the SPE Hydraulic Fracturing Technology Conference, The Woodlands, Texas, USA (2011). https://doi.org/10.2118/140514-MS
21. Weng, X.; Kresse, O.; Cohen, C.-E.; Wu, R.; Gu, H.: Modeling of hydraulic fracture network propagation in a naturally fractured formation. SPE Prod. Oper. **26**(04), 368–380 (2011). https://doi.org/10.2118/140253-pa
22. McClure, M.; Horne, R.N.: Discrete Fracture Network Modeling of Hydraulic Stimulation: Coupling Flow and Geomechanics. Springer, Berlin (2013)
23. Huang, J.; Safari, R.; Lakshminarayanan, S.; Mutlu, U.; McClure, M.: Impact of discrete fracture network (DFN) reactivation on productive stimulated rock volume: microseismic, geomechanics and reservoir coupling. In: Paper ARMA 2014-7017 Presented at the 48th U.S. Rock Mechanics/Geomechanics Symposium, Minneapolis, Minnesota (2014)
24. Sun, Y.: Impact of Slickwater Fracturing Fluid Compositions on the Petrophysical Properties of Shale and Tightsand. Missouri University of Science and Technology, Rolla (2014)
25. Economides, M.J.; Nolte, K.G.; Ahmed, U.; Schlumberger, D.: Reservoir Stimulation, vol. 18. Wiley, Chichester (2000)
26. England, A.; Green, A.: Some Two-Dimensional Punch and Crack Problems in Classical Elasticity, vol. 59. Cambridge University Press, Cambridge (1963)
27. Guo, J.; Lu, Q.; Zhu, H.; Wang, Y.; Ma, L.: Perforating cluster space optimization method of horizontal well multi-stage fracturing in extremely thick unconventional gas reservoir. J. Nat. Gas Sci. Eng. **26**, 1648–1662 (2015). https://doi.org/10.1016/j.jngse.2015.02.014

28. Liu, C.; Liu, H.; Zhang, Y.; Deng, D.; Wu, H.: Optimal spacing of staged fracturing in horizontal shale-gas well. J. Petrol. Sci. Eng. **132**, 86–93 (2015). https://doi.org/10.1016/j.petrol.2015.05.011
29. Guo, D.; Ji, L.; Zhao, J.; Liu, C.: 3-D fracture propagation simulation and production prediction in coalbed. Appl. Math. Mech. **22**(4), 385–393 (2001). https://doi.org/10.1023/a:1016337331556
30. Elbel, J.L.; Piggott, A.R.; Mack, M.G.: Numerical modeling of multilayer fracture treatments. In: Paper SPE 23982 Presented at the Permian Basin Oil and Gas Recovery Conference, Midland, Texas (1992). https://doi.org/10.2118/23982-MS
31. Crouch, S.: Solution of plane elasticity problems by the displacement discontinuity method. I. Infinite body solution. Int. J. Numer. Methods Eng. **10**(2), 301–343 (1976). https://doi.org/10.1002/nme.1620100206
32. Cheng, Y.: Boundary element analysis of the stress distribution around multiple fractures: implications for the spacing of perforation clusters of hydraulically fractured horizontal wells. In: Paper SPE 125769 Presented at the SPE Eastern Regional Meeting, Charleston, West Virginia, USA (2009). https://doi.org/10.2118/125769-MS
33. Wu, K.; Olson, J.E.: Investigation of the impact of fracture spacing and fluid properties for interfering simultaneously or sequentially generated hydraulic fractures. SPE Prod. Oper. **28**(04), 427–436 (2013). https://doi.org/10.2118/163821-pa
34. Schepers, K.C.; Gonzalez, R.J.; Koperna, G.J.; Oudinot, A.Y.: Reservoir modeling in support of shale gas exploration. In: Paper SPE 123057 Presented at the Latin American and Caribbean Petroleum Engineering Conference, Cartagena de Indias, Colombia (2009). https://doi.org/10.2118/123057-MS
35. Du, C.M.; Zhang, X.; Zhan, L.; Gu, H.; Hay, B.; Tushingham, K.; Ma, Y.Z.: Modeling hydraulic fracturing induced fracture networks in shale gas reservoirs as a dual porosity system. In: Paper SPE 132180 Presented at the International Oil and Gas Conference and Exhibition in China, Beijing, China (2010). https://doi.org/10.2118/132180-MS
36. Ozkan, E.; Raghavan, R.: New solutions for well test analysis problems: part 1-analytical considerations. SPE Form. Eval. **6**(03), 359–368 (1991). https://doi.org/10.2118/18615-pa
37. Stehfest, H.: Algorithm 368: numerical inversion of laplace transforms. Commun. ACM **13**(1), 47–49 (1970). https://doi.org/10.1145/361953.361969
38. Warpinski, N.R.: Hydraulic fracturing in tight, fissured media. J. Petrol. Technol. **43**(02), 146–209 (1991). https://doi.org/10.2118/20154-pa
39. Ren, L.; Lin, R.; Zhao, J.; Yang, K.; Hu, Y.; Wang, X.: Simultaneous hydraulic fracturing of ultra-low permeability sandstone reservoirs in China: mechanism and its field test. J. Cent. South Univ. **22**(4), 1427–1436 (2015). https://doi.org/10.1007/s11771-015-2660-1
40. Warpinski, N.R.; Teufel, L.W.: Influence of geologic discontinuities on hydraulic fracture propagation. J. Petrol. Technol. **39**(02), 209–220 (1987). https://doi.org/10.2118/13224-pa
41. Guo, T.; Li, J.; Lao, M.; Li, W.: Integrated geophysical technologies for unconventional reservoirs and case study within fuling shale gas field, Sichuan Basin, China. In: Paper SPE 178531 Presented at the Unconventional Resources Technology Conference, San Antonio, Texas, USA (2015). https://doi.org/10.2118/178531-MS
42. Zhao, J.; Li, Z.; Hu, Y.; Ren, L.; Tao, Z.: The impacts of microcosmic flow in nanoscale shale matrix pores on the gas production of a hydraulically fractured shale-gas well. J. Nat. Gas Sci. Eng. **29**(Supplement C), 431–439 (2016). https://doi.org/10.1016/j.jngse.2016.01.025